Scattering of sound by a vorticity filament: An experimental and numerical investigation

Sébastien Manneville,* Philippe Roux, Mickaël Tanter, Agnès Maurel, and Mathias Fink

Laboratoire Ondes et Acoustique, Université Denis Diderot, CNRS UMR No. 7587, École Supérieure de Physique et Chimie Industrielles, 10 rue Vauquelin, 75005 Paris, France

Frédéric Bottausci and Philippe Petitjeans

Laboratoire de Physique et Mécanique des Milieux Hétérogènes, CNRS UMR No. 7636, École Supérieure de Physique et Chimie Industrielles, 10 rue Vauquelin, 75005 Paris, France

A vorticity filament is investigated experimentally using the transmission of an ultrasonic wave through the flow. The analysis of the wave-front distortion provides noninvasive measurements of the vortex circulation and size. The latter is estimated by analytical calculations of the scattering of a plane wave by a vorticity filament. The case of a cylindrical wave incident on a vortex leads to similar experimental results which are successfully compared to a parabolic equation simulation. Finally, a finite-difference code based on linear acoustics is presented, in order to investigate the structure of the scattered wave numerically.

I. INTRODUCTION

The scattering of sound by a vortex has been the subject of intense research for more than 50 years. Such an intensive effort results from both experimental and theoretical motivation.

Experimentally, sound waves provide a *noninvasive* way to probe a flow. Indeed, techniques that allow spatial measurements without disturbing the flow are of great interest in aero- and hydrodynamics. An optical method such as laser Doppler velocimetry leads only to local measurements and particle imaging velocimetry is not well suited for large-scale experiments, e.g., in the atmosphere or ocean. Moreover, such optical techniques require a seeding of the flow by reflecting particles and they do not give access to any phase information on the wave. A sound wave, however, can be transmitted through a flow and the phase shift induced by the flow can be measured and analyzed. This transmission technique was first proposed by Schmidt and co-workers [1,2] and is now widely used in ocean acoustics for tomographic techniques [3,4]. More recently, the use of plane transducers [5–7] and the introduction of fully programmable transducer arrays [8,9] has led to spatial and dynamical characterization of isolated vortices. When the vortex size is large compared to the ultrasound wavelength, the phase shift is easily interpreted using geometrical acoustics and yields a direct measurement of the vortex circulation, size, and position.

Such noninvasive measurements are necessary to understand the structure, dynamics, and instabilities of an isolated, ''large'' vortex. However, more complex flows display vortical structures over a large range of spatial scales. For instance, turbulent flows were shown to contain structures with very intense, concentrated vorticity [10]. When sonicated with an acoustic wave, such ''vorticity filaments'' behave as line scatterers. Sound scattering by a single vorticity filament

has been intensively studied since publication of Lighthill's classical theory of aerodynamic sound [11–15]. Such approaches aim at computing the scattering cross section of a vortex in the Born limit (long-wavelength approximation). They are concerned with the two-dimensional (2D) interaction between an axisymmetric vortex and a sound wave propagating in a plane perpendicular to the vortex axis. In that case, the scattering pattern has a quadrupolar structure but also displays a singularity in the forward direction where the scattering amplitude diverges due to long-range refraction and advection effects. Theoretical and analytical refinements have recently been proposed to account for both sound scattering by the vortex core and long-range refraction effects [16,17]. In those two-dimensional calculations, the scattered pressure field is decomposed in partial waves that can be expressed as series of Bessel or Hankel functions. These are analogous to those that arise in the classical quantum mechanics problem of a beam of charged particles incident on a tube of magnetic field, a problem known as the ''Aharonov-Bohm effect'' [18]. This formal analogy with quantum mechanics was first introduced by Berry *et al.* [19] who proposed to study experimentally the scattering of surface waves by a vortex. A similar experiment was conducted very recently [20], which showed the validity of such an analogy and led to analytical developments in the case of surface waves [21]. The signature of ultrasound scattering by a single vortex was experimentally observed in water by Roux *et al.* [22], who checked that analytical calculations based on the quantum analogy also hold in acoustics; it was later observed in air by Pinton and Brillant [23].

For the sake of completeness, let us finally mention more general work on scattering of sound by random moving media [24,25]. When the flow is composed of a distribution of vortices, the scattered acoustic signal has been related to the spatial Fourier transform of the vorticity [26,27]. Such a spectral analysis of sound scattering has triggered experimental efforts to try to investigate turbulent flows using acoustics [28,29].

The aim of the present paper is to complete a previous

---

*Author to whom correspondence should be addressed. FAX: 33-140-794-468. Electronic address: sebastien.manneville@espci.fr
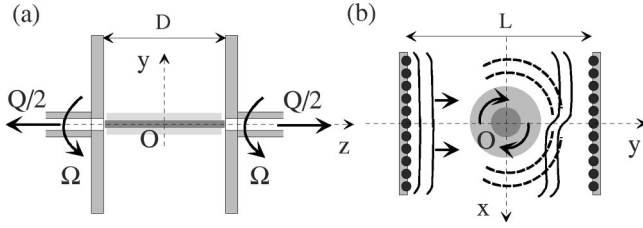
FIG. 1. Sketch of the experimental setup (a) in the (y,z) plane; (b) in the (x,y) plane: the incident plane wave emitted by the transducer array on the left is distorted and scattered by the vorticity filament.

paper [22] with an additional set of experiments on sound scattering by an isolated vorticity filament. The second part of this paper describes the experimental setup used to generate a vorticity filament and explains the acoustic technique. Section III is devoted to the estimation of the vortex circulation from the phase-shift data. Section IV deals with the scattering of a plane wave by a vorticity filament. We show that a nonintrusive measurement of the vortex size is possible by using analytical calculations based on the quantum analogy. In Sec. V, we focus on the case of a cylindrical incident wave. Experimental results are compared to a numerical simulation based on a parabolic equation. A finite-difference code is then used in Sec. VI to study the whole scattered pressure field.

II. EXPERIMENTAL SETUP AND ACOUSTIC TECHNIQUE

Our experiments rely on the transmission of an acoustic wave through a very thin and very intense vortex. Such a vorticity filament is generated in water between two coaxial, corotating disks (diameter 10 cm), a classical von Kármán geometry [30]. At the center of each disk, a symmetric suction is applied by pumping the water through small holes of diameter 5 mm. The suction enhances the vorticity induced by the disk rotation, which generates a strong vorticity filament between the two disks. The walls of the water tank are far enough from the disks so that the only control parameters are the disk rotation speed $\Omega/2\pi = 0-20$ Hz, the suction flow rate $Q = 0-6.4$ l/min, and the distance between the two disks $D = 2-30$ cm. The geometry of the experiment is sketched in Fig. 1. For more technical details about this hydrodynamic setup, the reader is referred to Refs. [31,32]. In any case, the water level above the vortex axis is large enough to prevent any degassing or cavitation. In particular, we checked that no air bubble was present inside the vortex core, so that the vorticity filament generated with this setup is always acoustically penetrable. Figure 2 shows a snapshot of the vortex visualized by injecting dyes directly inside the vortex core.

Let us now briefly recall the transmission technique used to characterize a vortex with ultrasound [7,8]. As shown in Fig. 1(b), a plane wave is emitted by a linear array of 64 piezoelectric transducers working at a central frequency of $f_0 = 3.5$ MHz. The element size is 0.39 mm along the x axis by 12 mm along the z axis, and the transducers are prefocused in the z direction at 70 mm. The array pitch is 0.42
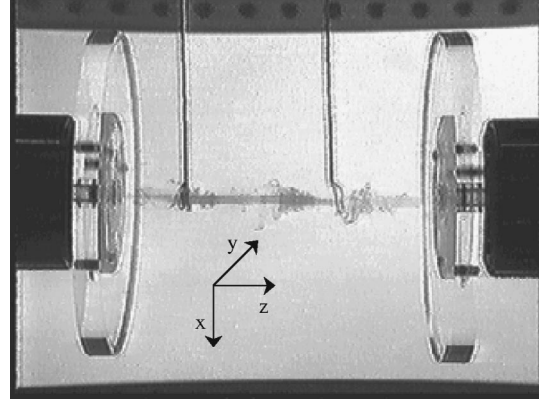

FIG. 2. Photograph of the vorticity filament visualized with two different dyes. The two vertical lines correspond to the dye injectors.

mm, leading to a total aperture of 27 mm. Each transducer has its own amplifier, an 8-bit digital-to-analog converter, a storage memory, and an 8-bit analog-to-digital converter working at 20 MHz. The plane wave propagates perpendicularly to the vortex axis in the (xy) plane and keeps a rather small extent (less than 10 mm) in the z direction because of the prefocusing. The experimental configuration is thus close to the 2D situation classically investigated in theoretical papers.

The acoustic signal $p(x,t)$ is recorded on another transducer array after one crossing of the flow as a function of time t and of the receiver position x. This signal is compared to the one obtained in the fluid at rest, $p_0(x,t)$, using a Fourier transform at the central frequency f_0:

$$\frac{\hat{p}(x,f_0)}{\hat{p}_0(x,f_0)} = A(x)e^{i\phi(x)}, \tag{2.1}$$

where the caret indicates the Fourier transform. Equation (2.1) defines the amplitude distortion $A(x)$ and the phase distortion $\phi(x)$ of the acoustic wave due to the vortex. Both the Fourier transforms in Eq. (2.1) are taken in the same time window. Moreover, this window is chosen to fit only the transmitted signal in order to remove spurious echoes corresponding to reflections at the tank boundaries. Since the transducers can work in both transmit and receive modes, simultaneous two-way transmissions are systematically used to compensate for the effects of temperature or density inhomogeneities in the medium and for possible mechanical vibrations of the setup [8,9,31]. The positions of the two arrays, in particular their distances to the z axis, are controlled by 3D MicroContrôle actuators. In Sec. V, we will also use a monoelement transducer to emit a cylindrical wave at 3.5 or 1.5 MHz. In that case, the phase and amplitude distortions are still defined by Eq. (2.1) but two-way transmissions are no longer possible. All the acoustic measurements are performed in the plane $z = D/6$ rather than at $z = 0$. Indeed, the stagnation point at $z_0 \approx 0$ [defined as the point on the z axis where the longitudinal velocity $u_z(z_0)$ is zero] fluctuates rapidly in time and the flow may present strong three-dimensional features in the plane $z = 0$.

The vorticity filament evolves on characteristic time scales of order 0.1 s, which are very long compared to the acoustic travel time over the distance L between the two transducer arrays and to the duration of emission (typically 10 μs). Therefore, in the following, the flow will be considered as frozen during one acoustic transmission. The propagation of sound through the vorticity filament can then be described in terms of two independent dimensionless parameters:

$$M = \frac{u}{c} \quad \text{and} \quad \beta = \frac{a}{\lambda}. \tag{2.2}$$

M is the Mach number of the flow, u the maximum tangential velocity of the vortex, and $c \approx 1500$ m/s the speed of sound in water. β is the ratio of the vortex radius a to the acoustic wavelength $\lambda \approx 0.4$ mm at 3.5 MHz and $\lambda \approx 1$ mm at 1.5 MHz. By convention, the vortex radius is defined by

$$u_\theta(a) = \max[u_\theta(r)] = u, \tag{2.3}$$

where u_θ denotes the tangential velocity and r the distance to the center of the vortex.

In our experiments, $u \approx 1$ m/s and $a \approx 1$ mm so that $M \approx 10^{-3}$ and $\beta \approx 1-3$. Thus, low Mach number approximations will hold throughout this paper, whereas neither the Born limit ($\beta \ll 1$) nor the geometrical acoustics approximation ($\beta \gg 1$) are valid here. In other words, when using our acoustic technique, we expect to observe both the effects of sound scattering by the vortex core and the long-range effects of the velocity field on the incident wave.

III. ACOUSTIC MEASUREMENT OF THE VORTEX CIRCULATION

Outside the vortex core, i.e., for $r > a$, the flow is nearly irrotational and almost two dimensional. The velocity field should thus be given by $\mathbf{u}(\mathbf{r}) = \Gamma/2\pi r \mathbf{e}_\theta$, where Γ is the vortex circulation and $\mathbf{e}_\theta$ is the tangential unit vector. This behavior was checked in previous experiments in similar geometries [9,33,34]. Such a velocity field is slowly variable in space and sound-vortex interaction may be accounted for in the framework of geometrical acoustics. Let us denote as $\mathbf{n}(\mathbf{r})$ the unit vector tangential to the acoustic ray at position $\mathbf{r}$. The presence of the flow leads to a local modification of the sound speed according to $c(\mathbf{r}) = c_0 + \mathbf{u}(\mathbf{r}) \cdot \mathbf{n}(\mathbf{r})$, where c_0 is the sound speed in water at rest. If the acoustic ray does not penetrate the vortex core, its direction is constant and equal to $\mathbf{n}(\mathbf{r}) = \mathbf{e}_y$ for a plane wave propagating along the y axis [35].

For small Mach numbers, using an expansion to first order in M, the phase distortion due to the vorticity filament is readily shown to be [22]

$$\phi(x) \approx \frac{2\pi f_0}{c_0^2} \int_{R(x)} \mathbf{u}(\mathbf{r}) \cdot \mathbf{e}_y dl \approx \frac{2\pi f_0}{c_0^2} \frac{\Gamma}{\pi} \arctan\left(\frac{L}{2x}\right), \tag{3.1}$$

where the integral is taken over the acoustic ray path $R(x)$ from the emitter to the receiver of abscissa x. Figure 3(a)
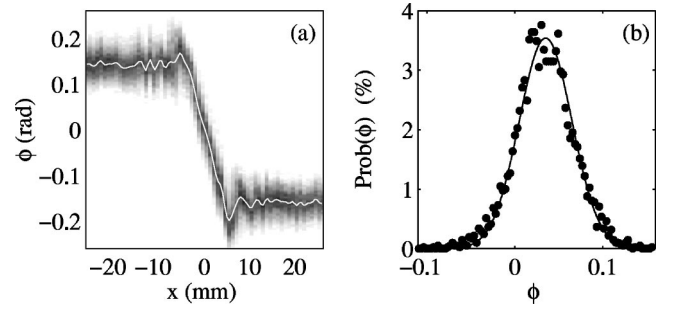

FIG. 3. (a) Average phase distortion $\langle \phi(x) \rangle_t$ in the presence of a vorticity filament. The gray scale corresponds to the probability of observing a given value of ϕ around the mean measurement. (b) Probability density function (PDF) of $\phi(x = -1 \text{ mm})$ (●). The solid curve is a Gaussian fit of the experimental PDF. The experimental conditions are 1024 plane emissions at $f_0 = 3.5$ MHz, $L \approx 200$ mm, $\Omega/2\pi = 5.0$ Hz, $Q = 3.7$ l/min, and $D = 80$ mm.

shows the typical phase distortion $\langle \phi(x) \rangle_t$ averaged over 1024 consecutive samples. The distance between the two transducer arrays is $L \approx 200$ mm and the incoming frequency is $f_0 = 3.5$ MHz. The origin $x = 0$ was chosen so that it coincides with the average position of the vortex center: $\langle \phi(x = 0) \rangle_t = 0$. A positive (negative) phase shift corresponds to a signal that has been sped up (slowed down) by the flow. For $|x| > 10$ mm, i.e., outside the vortical region, the phase shift remains constant. Indeed, when $|L/2x| \gg 1$, Eq. (3.1) becomes $\phi(x) = \text{sgn}(x)\pi f_0 \Gamma/c_0^2$. The phase jump $\Delta \phi$ between $x < -10$ mm and $x > 10$ mm is thus given by

$$\Delta \phi = \frac{2\pi f_0}{c_0^2} \Gamma. \tag{3.2}$$

Using Eq. (3.2), the vortex circulation is easily measured within a few percent. The measurements of Fig. 3(a) lead to $\Gamma = 330 \pm 10 \text{ cm}^2/\text{s}$.

Note that in the Rankine model, for which $u_\theta(r) = \Gamma/2\pi r$ for $r \geq a$ and $u_\theta(r) = \Gamma r/2\pi a^2$ for $r \leq a$, $\Gamma = 2\pi u a$ so that

$$\frac{\Delta \phi}{2\pi} = 2\pi M\beta \equiv \alpha. \tag{3.3}$$

α measures the amplitude of the phase jump and is called the "dislocation parameter." When $\alpha > 1$, the wave front is "dislocated" in the sense that the vortex is strong enough to distort the wave front by more than one wavelength. In that case, additional wave fronts appear in the pressure field to compensate for such large phase jumps. The value of Γ inferred from Fig. 3(a) corresponds to a rather small value of the dislocation parameter $\alpha \approx 0.05$. Our experimental situation is thus slightly different from the one investigated by Vivanco et al. [20], where high values of the dislocation parameter ($\alpha \approx 1$) are achieved using surface waves.

As shown in Fig. 3, the fluctuations of the phase distortion around $\langle \phi(x) \rangle_t$ are rather large, of order 25%. Such fluctuations are much larger than the noise level of the data and can be attributed to the nonstationarity of the flow [31]. Indeed,
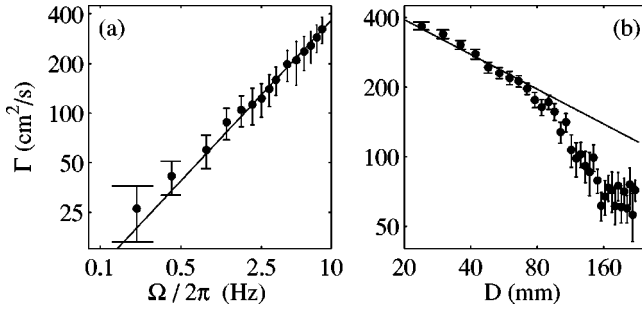
FIG. 4. Mean circulation of the vorticity filament as a function of (a) the rotation speed of the disks Ω (for $Q=3.0$ l/min and $D=120$ mm) and (b) the distance D between the two disks (for $\Omega/2\pi=1.7$ Hz and $Q=5.5$ l/min). Note the logarithmic scales and the error bars, which represent the data standard deviation. Solid lines correspond to power laws with exponents 0.75 and -0.5.

the vorticity filament constantly undergoes a more or less regular precession motion around the rotation axis of the disks. This precession motion depends on the control parameters and can be studied using acoustics by following the position of the vortex [32]. Moreover, the Reynolds number based on the disk radius can reach values as high as 10^5 so that some part of the flow may be turbulent even if the vortex always remains coherent. It is therefore not surprising to observe a Gaussian statistics for the phase fluctuations [see Fig. 3(b)].

The next section will show how important it is to compensate for the vortex motion in order to interpret correctly the phase distortion for $|x|<10$ mm. However, the raw average $\langle\phi(x)\rangle_t$ allows one to measure the mean circulation of the vortex as a function of the control parameters Ω and D, as shown in Fig. 4. Those results show that

$$\Gamma\propto\frac{\Omega^{0.75}}{D^{0.5}}.\tag{3.4}$$

The power law dependence on Ω, with an exponent close to $\frac{3}{4}$ for $\Omega=0.5$–10 Hz, differs from the behavior as $\Omega^{1/2}$ predicted and observed in confined flows [33,36]. However, it is consistent with the results of Ref. [37] obtained with counter-rotating disks, which show that $\Gamma\propto\Omega^{0.8}$. The fact that Γ scales as $D^{-1/2}$ over the range $D=20$–80 mm can be explained by simple energetic considerations [32]. The departure from the power law behavior for larger values of D results from an instability of the vorticity filament. Indeed, when the distance between the disks is increased, the vortex may undergo breakdowns that lead to a lower mean circulation.

In order to track such an instability in the control parameter space, we define a ''probability of presence'' of the vortex by counting the proportion of phase measurements that display a phase jump similar to that of Fig. 3(a). Such phase distortions are characteristic of the presence of a vorticity filament. For a given set of control parameters, the probability of presence is computed from 1024 measurements recorded in about 2 min. Such a sample is long enough to yield a good statistical characterization of the vorticity filament. The resulting stability diagram in the (Q,D)
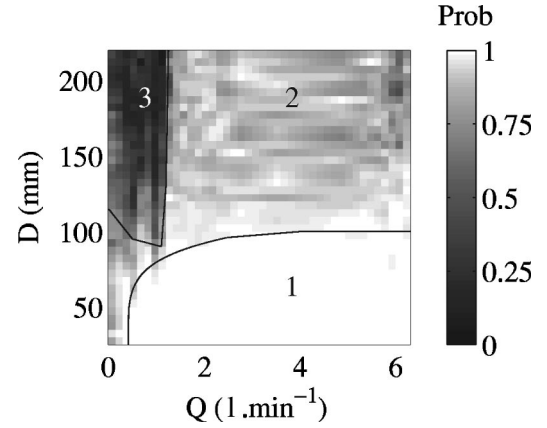

FIG. 5. Stability diagram of the vorticity filament in the (Q,D) plane. The gray scale corresponds to the probability of presence of the vorticity filament computed from 1024 consecutive measurements of the phase distortion for $\Omega/2\pi=0.8$ Hz.

plane is shown in Fig. 5 for a given value of Ω. Three different domains can be qualitatively distinguished. When the suction is large and the disks are close to each other ($D<100$ mm), the probability of presence is 1 (domain 1). However, the probability decreases down to values of order 0.5 when Q is decreased or when D is increased (domain 2). In that case, the vorticity filament goes unstable from time to time and the phase distortion does not always display a phase jump. A very sharp transition is observed between domain 2 and domain 3 where the vorticity filament almost never shows up. Indeed, when the suction is too weak and the distance D too large, the vorticity injected in the flow by the disk rotation is not amplified to form a vorticity filament and jumps are never observed in the phase distortion.

Lastly, the vortex circulation can be measured from the phase distortions as a function of time. Such dynamical measurements were performed with a 30 Hz sampling rate in the case of the transient regime of formation of the vorticity filament. Figure 6(a) presents a spatiotemporal diagram of the phase measurements after the rotation and the suction are applied simultaneously at time $t_0=6$ s. The phase distortion goes from zero to the typical phase jump within about 5 s. Figure 6(b) shows that the wave front is first only bent due to
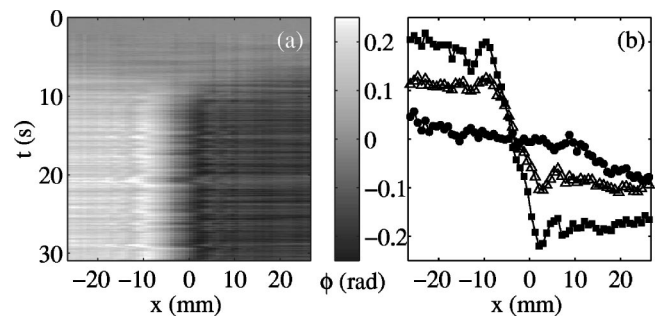

FIG. 6. Transient regime during the formation of the vorticity filament. (a) Phase distortions $\phi(x)$ measured as a function of time and coded in gray levels. (b) $\phi(x)$ at $t=6.5$ ($\bullet$), 9.8 ($\triangle$), and 13.1 s ($\blacksquare$). $\Omega/2\pi=6.7$ Hz, $Q=5.7$ l/min, and $D=80$ mm. Rotation and suction are turned on at $t_0=6$ s.
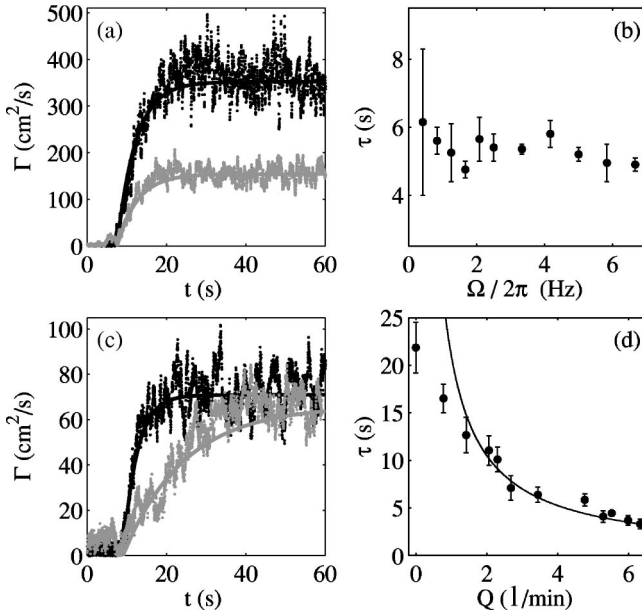
FIG. 7. Transient regimes of formation. (a) Vortex circulation $\Gamma(t)$ for $\Omega/2\pi=2.1$ Hz (gray) and $\Omega/2\pi=6.7$ Hz (black). Solid lines are exponential fits of the form $\Gamma(t+t_0)=\Gamma_0[1-\exp(-t/\tau)]$ with $\tau=5.0$ and 4.7 s, respectively. Γ_0 is the final value of the circulation. (b) Characteristic time $\tau(\Omega)$ for $Q=5.7$ l/min and $D=80$ mm. (c) $\Gamma(t)$ for $Q=0.7$ (gray) and 6.3 l/min (black). The solid lines are computed with $\tau=17$ and 9 s, respectively. (d) $\tau(Q)$ for $\Omega/2\pi=0.8$ Hz and $D=80$ mm. The solid line represents a fit with $\tau\propto1/Q$. Rotation and suction are turned on at $t_0=6$ s in (a) and 8 s in (b).

the solid body rotation induced by the disk rotation. The vorticity is then amplified by the pumping and concentrates in the vortex core to form the vorticity filament. For $t>15$ s, after the transient regime, the precession motion of the vortex can be detected in the fluctuations of $\phi(x)$. Figure 7 displays the evolution of the vortex circulation $\Gamma(t)$ deduced from the phase measurements during various transient regimes of formation. In Figs. 7(a) and 7(b), the rotation speed Ω of the disks is varied for a fixed suction flow rate Q, whereas, in Figs. 7(c) and 7(d), Q is varied for a given value of Ω. For each set of control parameters, the curve $\Gamma(t)$ is well fitted by an exponential relaxation, which defines a characteristic growth time τ for the circulation. Figures 7(b) and 7(d) show that τ is almost independent of Ω but strongly decreases with Q. Even if rotation and stretching are never completely independent [36], this result means that in this experiment the formation of the vorticity filament is mainly governed by the suction flow rate. The rotation thus dictates only the asymptotic value Γ_0 of the circulation [compare Figs. 7(a) and 7(c)]. Indeed, from the vorticity equation, one gets [38]

$$\frac{\partial\omega_z}{\partial t}\approx\omega_z\frac{\partial u_z}{\partial z}, \qquad (3.5)$$

where ω_z is the component of the vorticity $\boldsymbol{\omega}=\boldsymbol{\nabla}\times\mathbf{u}$ along the z axis. The ''stretching'' $\gamma=\partial u_z/\partial z$ appears as the inverse of a characteristic time. A rough estimate for the
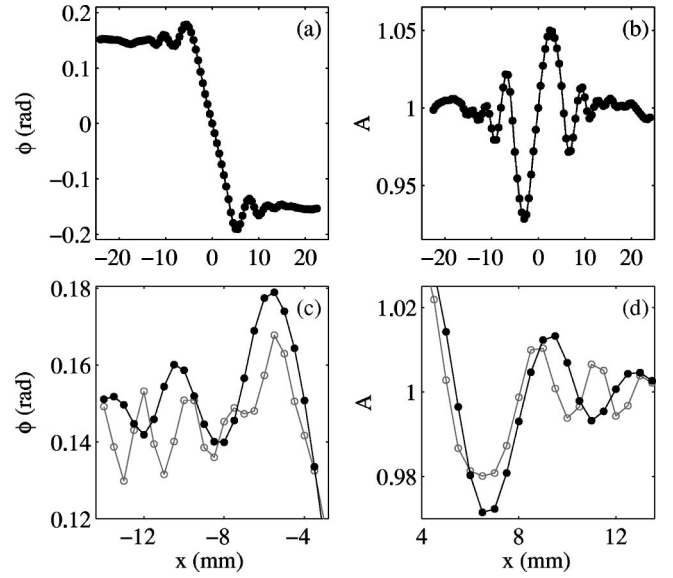

FIG. 8. Compensation of the vortex motion. (a) Mean phase distortion $\langle\phi(x-x_0(t))\rangle_t$ and (b) mean amplitude distortion $\langle A(x-x_0(t))\rangle_t$ averaged in the vortex frame of reference. (c) $\langle\phi(x-x_0(t))\rangle_t$ ($\bullet$ and black line) compared to $\langle\phi(x)\rangle_t$ ($\circ$ and gray line). (d) $\langle A(x-x_0(t))\rangle_t$ ($\bullet$ and black line) compared to $\langle A(x)\rangle_t$ ($\circ$ and gray line). Same experimental conditions as in Fig. 3.

stretching is $\gamma\propto 2u_z(z=D/2)/D\approx Q/DS$, where S denotes the surface of the suction hole. Since $\tau\propto1/\gamma$, one expects that $\tau\propto D/Q$, in good agreement with Fig. 7(d), where τ is shown to scale as $1/Q$ for large value of Q. Once again, for the smallest flow rates, the vortex may be unstable so that $\tau(Q)$ may depart from this simple behavior.

IV. SCATTERING OF A PLANE WAVE

In the previous section, we used an approach based on geometrical acoustics to account for the phase jump $\Delta\phi$. This approach is valid outside the vortex core where the flow is slowly varying in space. Here, we show that this first effect (the phase jump) goes along with an effect due to scattering of the incoming ultrasound by the vortex core.

As previously mentioned in Refs. [20,22], sound scattering leads to oscillations in the phase distortion that are superimposed on the phase jump. Those oscillations can be interpreted as an interference pattern between the distorted incident wave and the scattered wave. In the present experiment, the very small radius of the vortex should allow sound scattering to take place. However, oscillations are not clearly visible in the raw average $\langle\phi(x)\rangle_t$ of Fig. 3(a). Indeed, due to the precession motion of the vortex, oscillations cancel out when the phase measurements are averaged over 1024 samples without any further data analysis. In order to take into account the precession motion, we first measure the position of the vortex center along the x axis. This position is obtained from each phase measurement ϕ by detecting the abscissa x_0 for which $\phi(x_0)=0$. This procedure yields a time series $x_0(t)$ and the phase distortions are then averaged *in the vortex frame of reference* by computing
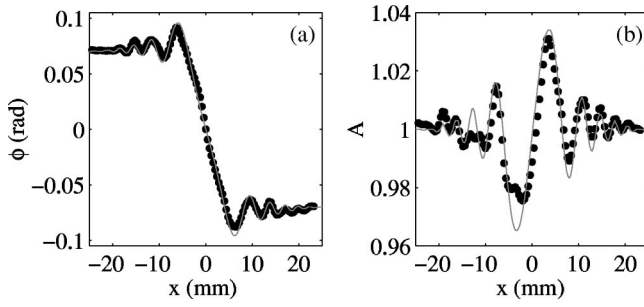
FIG. 9. Comparison between experimental data (●) averaged in the vortex frame of reference and the analytical calculations for $\Gamma = 145$ cm^2/s and $a = 1.3$ mm (gray lines). (a) Phase distortion. (b) Amplitude distortion. The experimental conditions are 1024 plane emissions at $f_0 = 3.5$ MHz, $L = 240$ mm, $\Omega/2\pi = 1.7$ Hz, $Q = 5.9$ l/min, and $D = 80$ mm.
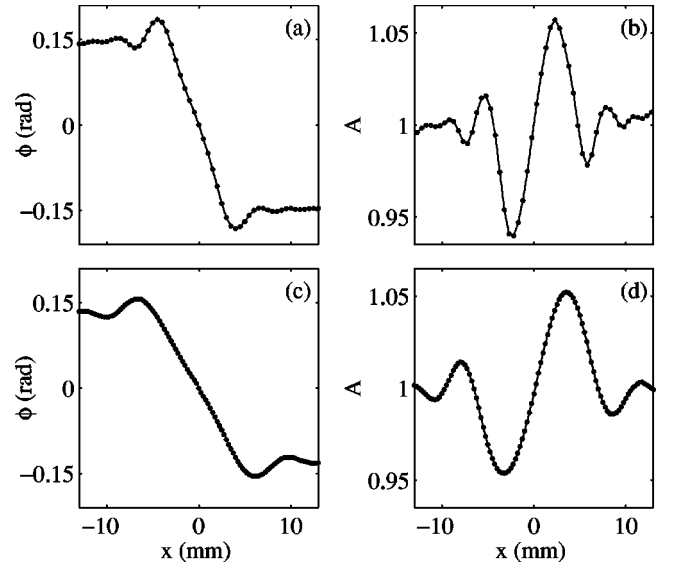

FIG. 10. Influence of the incident wave form. (a) Phase and (b) amplitude distortions averaged in the vortex frame of reference for a plane incident wave and (c), (d) for a cylindrical incident wave. The experimental conditions are 4096 emissions at $f_0 = 3.5$ MHz, $L = 120$ mm, $\Omega/2\pi = 5.0$ Hz, $Q = 3.7$ l/min, and $D = 80$ mm.

$\langle \phi(x - x_0(t)) \rangle_t$. Figure 8 reveals well-defined oscillations in both the phase and the amplitude distortions when such a dynamical analysis is applied to the experimental data. In Figs. 8(c) and 8(d), averaging in the vortex frame of reference is compared to the raw averaging used in Fig. 3(a). Even if the values reached far from the vortex core are the same, the signals are much smoother and the oscillations much better defined when one compensates for the vortex motion.

Analytical calculations are available for the scattering of an infinite plane wave generated at infinity and incident on a Rankine vortex [19,21] or, equivalently, for scattering by a penetrable tube of magnetic field [39]. Such calculations are compared to experimental data in Fig. 9. The distance L_{em} (L_{rec}) between the z axis and the emitter (receiver) array is tuned to $L_{\text{rec}} = L_{\text{em}} = L/2 = 120$ mm. The vortex circulation Γ is first measured from the phase jump as in Sec. III. Thus, the only adjustable parameter in the analytical calculation is the vortex radius a. Very good fits of both the phase and amplitude distortions are obtained with $a = 1.3 \pm 0.1$ mm, which corresponds to $\beta \approx 3$. Note that such a measurement of the size of the vortex core is impossible with standard hot wire probes and would be very difficult with Doppler techniques due to particle demixing in the core [34].

In the far field region and outside an angular sector around the forward direction, more precisely for $(2\pi kr)^{1/2} \gg 1$ and $\pi - |\theta| \gg 1/(kr)^{1/2}$, the analytical expression of the pressure field reduces to [19]

$$p(r,\theta) \propto e^{-ikr\cos\theta + i\alpha\theta} + F(\theta)\sin(\pi\alpha)\frac{e^{ikr}}{\sqrt{2i\pi kr}}, \quad (4.1)$$

where $F(\theta) = \exp(i\theta/2)/i\cos(\theta/2)$. k is the wave number and θ the polar angle between $-\mathbf{e}_y$ and the direction of observation $\mathbf{r}$. The first term of the sum in Eq. (4.1) describes the distortion of the plane incident wave: the phase term $\alpha\theta$ corresponds exactly to the phase distortion given by Eq. (3.1). The second term represents the scattered wave and leads to the oscillations in $\phi(x)$ and $A(x)$.

V. SCATTERING OF A CYLINDRICAL WAVE

The above interpretation in terms of interference between the incident wave and the scattered wave still holds for a cylindrical incident wave. Due to the large aspect ratio of our transducers ($\approx 0.5 \times 10$ mm^2), we shall assume that the acoustic field emitted by a single transducer is mainly two dimensional and call it "cylindrical." Figure 10 compares the experimental results obtained at $f_0 = 3.5$ MHz with plane and cylindrical incident waves. Due to the divergent nature of the cylindrical wave, the wavelength of the oscillations in the wave-front distortion is bigger than with a plane wave. Moreover, the use of a single emitting element allows us to use a receiver array of 127 transducers with a pitch of 0.42 mm. The number of experimental points per oscillation is thus larger with a cylindrical emission [Figs. 10(c) and 10(d)] than with a plane emission [Figs. 10(a) and 10(b)]. In other words, a cylindrical emission provides a "zoom" on the vortex core and may lead to better precision in estimation of the vortex size.

However, to our knowledge, no analytical calculation is available in the literature in the case of a cylindrical wave emitted at a finite distance from a vortex. In order to interpret our data, we were led to implement a monochromatic numerical simulation based on a 2D parabolic equation. Previous numerical studies using parabolic equations dealt with the well-documented case of a plane incident wave [40,41]. Our numerical code was described and tested in a previous paper [42]. It relies on the resolution of the inhomogeneous Helmholtz equation

$$\nabla^2 p + k^2(\mathbf{r})p = S(\mathbf{r}), \quad (5.1)$$

where $S(\mathbf{r})$ corresponds to the acoustic sources and the local wave number $k(\mathbf{r}) = 2\pi f_0/[c_0 + \mathbf{u}(\mathbf{r}) \cdot \mathbf{n}(\mathbf{r})]$ results from the

sound-flow interaction. This expression for $k(\mathbf{r})$ is valid for small Mach numbers and for $\beta \gg 1/2\pi$. Equation (5.1) is solved in the forward direction $y > 0$ using the parabolic equation

$$\frac{\partial p}{\partial y} = i k_0 \sqrt{1 + \mathbf{K}(\mathbf{r})} \, p, \tag{5.2}$$

where $\mathbf{K}(\mathbf{r}) = [\partial^2/\partial x^2 + k^2(\mathbf{r}) - k_0^2]/k_0^2$ and $k_0 = 2\pi f_0/c_0$. The numerical scheme uses the split-step Padé solution proposed by Collins [43]. Higher-order Padé approximations of $[1 + \mathbf{K}(\mathbf{r})]^{1/2}$ provide a good numerical convergence for propagation angles up to 85° away from the y axis. The first-order differential equation (5.2) is solved from the emission plane $y = -L_{\mathrm{em}}$ to $y = L_{\mathrm{rec}}$ with a step $\delta y = \lambda$. The discretization along the x axis is $\delta x = \lambda/10$. The fluid velocity field is a Burgers vortex

$$u_\theta(r) = \frac{\Gamma}{2\pi r}(1 - e^{-r^2/4r_0^2}), \tag{5.3}$$

where r_0 is proportional to the vortex radius $a \approx 2.24 r_0$ and is given by $r_0 = (\nu/\gamma)^{1/2}$, where ν is the fluid kinematic viscosity and γ is the stretching. For a cylindrical wave emitted at position $\mathbf{R}$, the direction of propagation is taken to be $\mathbf{n}(\mathbf{r}) = (\mathbf{r} - \mathbf{R})/\|\mathbf{r} - \mathbf{R}\|$ even in the presence of the vortex. This assumption is valid provided that $M \ll 1$.

The cylindrical wave is emitted from $\mathbf{R} = -L_{\mathrm{em}} \mathbf{e}_y$. The phase and amplitude distortions are computed at $y = L_{\mathrm{rec}}$ from the pressure fields simulated in the presence of a vorticity filament and in the fluid at rest. By tuning Γ and a, a very good agreement with the experiment is obtained, as shown in Fig. 11 for $f_0 = 3.5$ and 1.5 MHz. The characteristics of the vortex are estimated within $\pm 5\%$. Due to the larger wavelength and smaller vortex size, the measurements at $f_0 = 1.5$ MHz correspond to $\beta \approx 1$. This value constitutes a physical limit of resolution of our technique. Indeed, we checked that for vortices of constant circulation but of different sizes below the acoustic wavelength ($\beta \le 1$), the wave-front distortions are very close to each other. In particular, the amplitude of the oscillations saturates, so that $\phi(x)$ and $A(x)$ vary significantly only for $\beta \ge 1$.

The agreement between the simulation and the experiment is confirmed in Figs. 12 and 13 where the distances L_{rec} and L_{em} are successively varied. Varying L_{rec} (Fig. 12) gives a picture of the wave-front distortion in two dimensions as the receiver gets farther from the vortex. Varying L_{em} (Fig. 13) helps to understand the convergence of the case of a cylindrical emission toward the case of a plane emission. Indeed, one expects that the results obtained with a plane incident wave will be recovered when $L_{\mathrm{em}} \to \infty$. Moreover, it is reasonable to assume that the far field solution takes a simple expression similar to Eq. (4.1). Let us postulate that, for $(2\pi kr)^{1/2} \gg 1$ and $\pi - |\theta| \gg 1/(kr)^{1/2}$, the pressure field can be written as the sum of a distorted cylindrical wave and a scattered wave. By using Eq. (3.1) and $\oint \mathbf{u} \cdot d\mathbf{l} = 0$ for a given closed path inside the irrotational region of the flow, it is easy to show that the phase distortion of a cylindrical wave is independent of L_{em} and is given by $\alpha\theta$ as in the plane
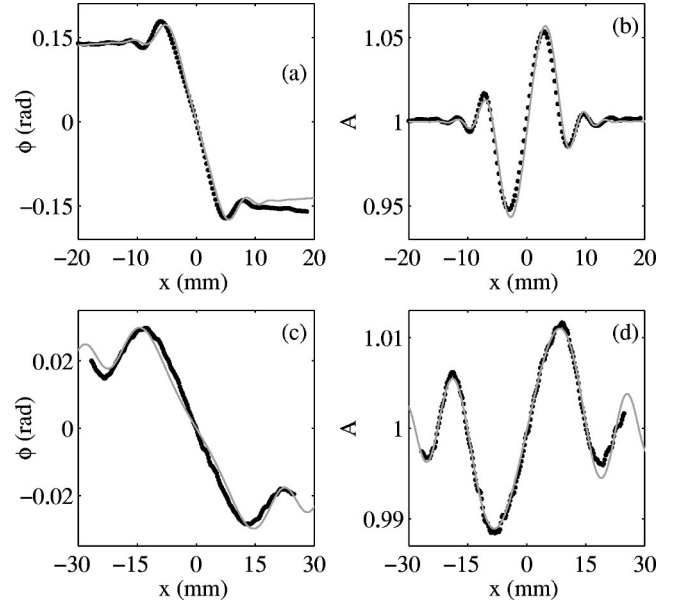

FIG. 11. Comparison between experimental data (●) averaged in the vortex frame of reference and the parabolic equation simulation (gray lines). (a) Phase and (b) amplitude distortions for a cylindrical emission at $f_0 = 3.5$ MHz with $L = 180$ mm, $\Omega/2\pi = 5.0$ Hz, $Q = 3.7$ l/min, $D = 80$ mm, and disks of diameter 10 cm. Simulation for a Burgers vortex [Eq. (5.3)] with $\Gamma = 310$ cm^2/s and $a = 1.35$ mm. (c) Phase and (d) amplitude distortions for a cylindrical emission at $f_0 = 1.5$ MHz with $L = 210$ mm, $\Omega/2\pi = 3.0$ Hz, $Q = 3.1$ l/min, $D = 30$ mm, and disks of diameter 5 cm. Simulation with $\Gamma = 112$ cm^2/s and $a = 0.9$ mm.

wave case. Taking into account the attenuation of the incident wave with distance leads to the following expression for the pressure field:

$$p(r, \theta) \propto \frac{e^{-ikr' + i\alpha\theta}}{\sqrt{2i\pi kr'}} + G(\theta, L_{\mathrm{em}}) \sin(\pi\alpha) \frac{e^{ikr}}{\sqrt{2i\pi kr}}, \tag{5.4}$$

where $r' = \|\mathbf{r} - \mathbf{R}\|$. Here, the amplitude G of the scattered wave depends on both θ and L_{em}. The simplest way to ac-
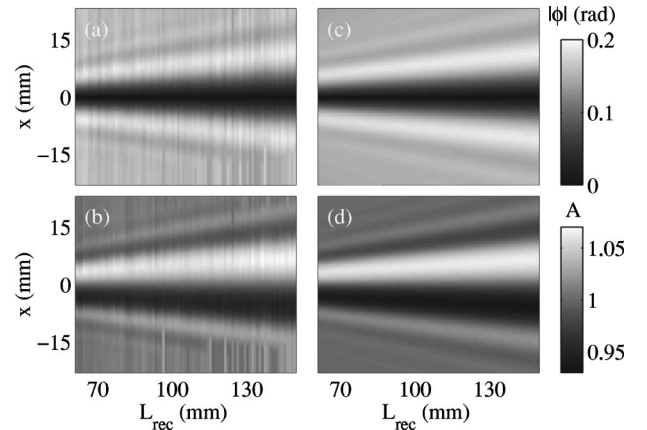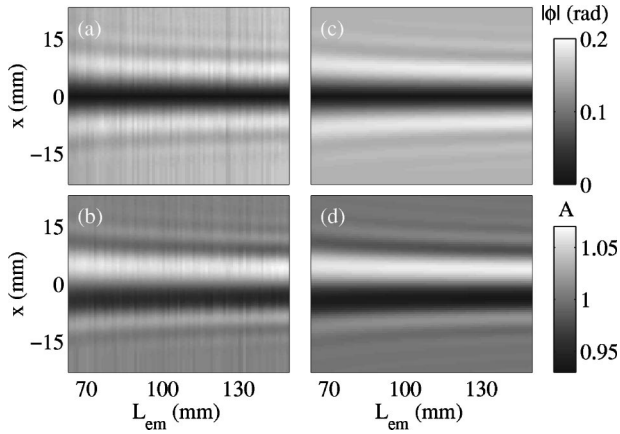

FIG. 12. Influence of the receiver position for a cylindrical emission at $f_0 = 3.5$ MHz. (a) Experimental phase and (b) amplitude distortions with $L_{\mathrm{em}} = 90$ mm, $\Omega/2\pi = 5.0$ Hz, $Q = 3.7$ l/min, $D = 80$ mm. (c), (d) Simulation with $\Gamma = 325$ cm^2/s and $a = 1.35$ mm.

FIG. 13. Influence of the emitter position for a cylindrical emission at $f_0 = 3.5$ MHz. (a) Experimental phase and (b) amplitude distortions with $L_{rec} = 90$ mm, $\Omega/2\pi = 5.0$ Hz, $Q = 3.7$ l/min, $D = 80$ mm. (c),(d) Simulation with $\Gamma = 325$ cm^2/s and $a = 1.35$ mm.

count for this dependence is to take $G(\theta, L_{em}) = F(\theta)/(2i\pi k L_{em})^{1/2}$ where $F(\theta)$ is given in Sec. V. Such a dependence means that the scattered wave is the same as in the plane wave case. Its amplitude has only been rescaled by the amplitude of the incident wave at $r = 0$ (using $r' = L_{em}$ at $r = 0$). As shown in Fig. 14, Eq. (5.4) provides a rather good prediction for the oscillations in $\phi(x)$ and $A(x)$. Since $r' \sim L_{em}$ when $L_{em} \to \infty$, G is also consistent with the fact that Eq. (5.4) should tend toward the plane wave case as $L_{em} \to \infty$. However, the oscillations predicted by Eq. (5.4) are slightly out of phase with the results of the simulation for large values of x. This may indicate that G also depends on the vortex radius a and that the variation of the curvature of the incident wave front with size a plays a significant role.

VI. NUMERICAL INVESTIGATION OF THE SCATTERED WAVE

The parabolic equation used in the previous section allows us to account for scattering around the forward direction. It is thus very well suited for modeling our transmission
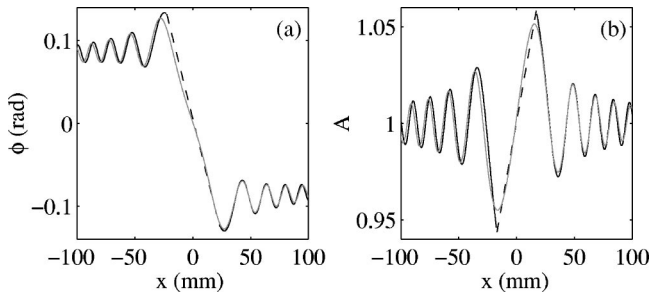

FIG. 14. Comparison between the parabolic equation simulation with $\Gamma = 470$ cm^2/s and $a = 0.5$ mm (gray lines) and the prediction of Eq. (5.4) with $\alpha = 0.03$ (black solid and dashed lines). (a) Phase and (b) amplitude distortions for a cylindrical emission at $f_0 = 1.5$ MHz with $L_{em} = 50$ mm and $L_{rec} = 200$ mm. The dashed lines are linear interpolations for the values of x where Eq. (5.4) is not valid.

experiments. However, if one wants to study the whole scattered pressure field, in particular at angles $|\theta| > 85°$, one has to use another numerical technique. For instance, finite-difference schemes take into account any direction of sound propagation. Whereas other investigators used direct numerical simulations of the full Navier-Stokes or Euler equations [44–46], we developed a code for linear acoustics in a moving medium. Our approach discriminates between a stationary, incompressible basic flow $(\mathbf{u}, P_0, \rho_0)$ and an acoustic perturbation $(\mathbf{v}, p, \rho)$. The density of the basic flow is assumed to be constant and the acoustic pressure and density are linked by the equation of state $p = \rho c_0^2$. Linearizing the Navier-Stokes equations and neglecting all terms of order M^2 lead to the following coupled equations [47]:

$$\nabla^2 p - \frac{1}{c_0^2}\frac{\partial^2 p}{\partial t^2} = -2\rho_0 \frac{\partial^2}{\partial x_i \partial x_j}(u_i v_j) + S(\mathbf{r}, t), \quad (6.1a)$$

$$\frac{\partial \mathbf{v}}{\partial \mathbf{t}} + (\mathbf{u} \cdot \nabla)\mathbf{v} + (\mathbf{v} \cdot \nabla)\mathbf{u} = -\frac{\nabla p}{\rho_0}. \quad (6.1b)$$

In Eq. (6.1a), the sound-flow interaction appears as a source term which involves the acoustic velocity $\mathbf{v}$. Thus, the problem has to be solved for both the variables p and $\mathbf{v}$. The 2D version of Eq. (6.1) is discretized over a rectangular grid of mesh $\delta x = \delta y = \lambda/12$ with $2^{10} \times 2^{10}$ points. The time step is $\delta t = 1/20 f_0$, so that the von Neumann stability criterion $\delta t \leq \delta x/c_0\sqrt{2}$ is satisfied. A second-order scheme is used to estimate the derivatives in Eq. (6.1a). Higher-order absorbing boundary conditions as in Ref. [48] limit the amplitude of waves reflected at the grid boundaries to -45 dB.

It can be shown that Eq. (6.1) is valid for $\beta \gg M/2\pi$ [31]. Since $M \ll 1$, it is more general than Eq. (5.1). In the monochromatic regime and when $\beta \gg 1/2\pi$, Eqs. (6.1) and (5.1) are equivalent and we checked that the results obtained in the forward direction with the parabolic equation and with the finite-difference code coincide. In spite of much longer computation times, the advantage of the finite-difference approach is to give access to the pressure field in time and for any direction of propagation. Figure 15 shows the propagation of a cylindrical pulse $p(x, y, t)$ through a Burgers vortex for $M = 0.1$ and $\beta = 0.5$. As seen in Figs. 15(b) and 15(c), the incident wave front is clearly distorted by the vortex core. The scattered wave is small compared to the incident pressure and can hardly be observed in Fig. 15(c).

A standard way to focus on the scattered wave is to study the difference $p_{scatt} = p - p_0$, where p_0 is the reference acoustic pressure computed in the fluid at rest. This is supposed to get rid of the incident wave front $p_{inc} \approx p_0$. However, as shown in Figs. 15(d)–15(f), this definition does not allow a better observation of the wave scattered by a Burgers vortex. Indeed, p_{scatt} contains not only the contribution of the scattered wave but also the effects of the advection due to the long-range nature of the Burgers velocity field $u_\theta(r) \sim 1/r$ as $r \to \infty$. This explains why p_{scatt} is always of the order of the incident pressure: even before the incident pulse crosses the vortex, $p \neq p_0$ due to advection effects [Fig. 15(d)]. Note that in Ref. [44] those effects are referred to as ''refraction''
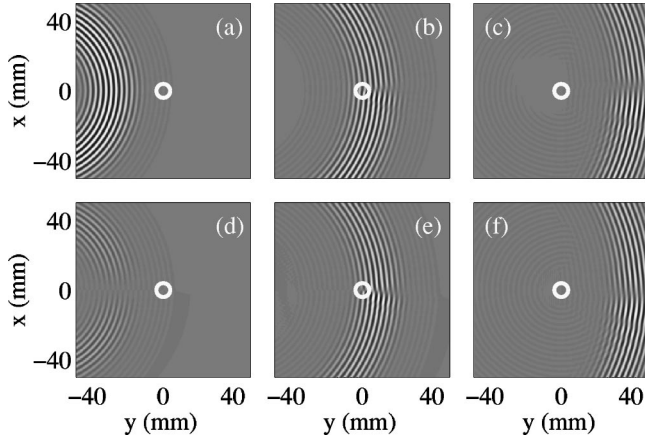
FIG. 15. Propagation of a cylindrical pulse through a Burgers vortex [Eq. (5.3)] with $M=0.1$ and $\beta=0.5$. Acoustic pressure field $p(x,t)$ at $t=$(a)55, (b) 80, and (c) 105 μs. ''Scattered'' pressure field $p_{\rm scatt}=p-p_0$ at $t=$(d) 55, (e) 80, and (f) 105 μs. The vortex rotates clockwise and its center is indicated by a white circle. The cylindrical wave (eight acoustic periods at $f_0=500$ kHz) is emitted from $L_{\rm em}=-75$ mm. The pressure is coded using a linear gray scale. In (a)–(c), black corresponds to the minimum pressure and white to the maximum pressure. In (d) and (e), $p_{\rm scatt}$ has been rescaled by the maximum value obtained in (f).

effects, which is rather ambiguous since the flow is irrotational for $r>a$ and acoustic rays are not deflected by irrotational flows. In Fig. 15(f), the effects of advection mask the scattered wave, which is about 100 times smaller. Let us finally mention that advection also affects the scattered wave at large distances from the vortex core.

In order to avoid such effects of a slowly decaying velocity field, one may use a vortex with vanishing circulation. As mentioned by Colonius, Lele, and Moin [44], the Taylor vortex, whose velocity field decays exponentially fast,

$$u_\theta(r)=u\frac{r}{a}\exp\left[\frac{1}{2}\left(1-\frac{r^2}{a^2}\right)\right], \qquad (6.2)$$

allows one to minimize ''refraction'' effects. Figure 16(a) shows that, with a Taylor vortex, $p_{\rm scatt}$ is zero everywhere before the incident wave crosses the vortex core. Thus, in Figs. 16(b) and 16(c), $p_{\rm scatt}$ corresponds to the pressure field scattered away from a Taylor vortex. It is clear that the scat-
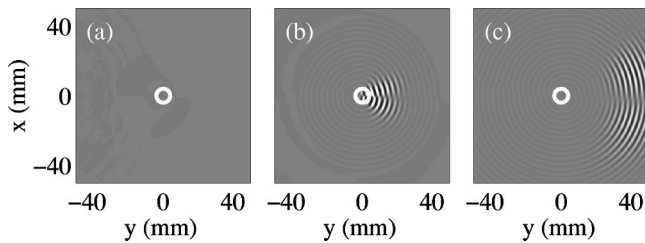

FIG. 16. Propagation of a cylindrical pulse (eight acoustic periods at $f_0=500$ kHz) through a Taylor vortex [Eq. (6.2)] with $M=0.1$ and $\beta=0.5$. ''Scattered'' pressure field $p_{\rm scatt}=p-p_0$ at $t=$(a) 55, (b) 80, and (c) 105 μs. In (a) and (b), $p_{\rm scatt}$ has been rescaled by the maximum value obtained in (c).
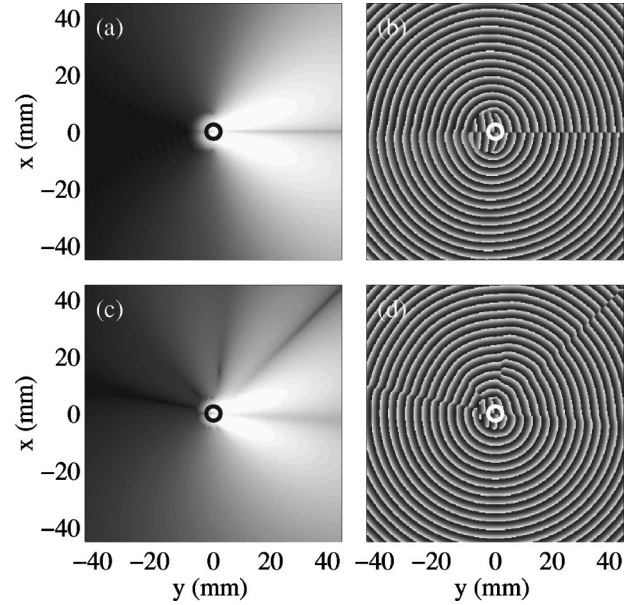

FIG. 17. Pressure field scattered by a Taylor vortex for a monochromatic cylindrical incident wave. (a) Amplitude and (b) phase of $p_{\rm scatt}$ for $M=10^{-4}$ and $\beta=0.5$. (c) Amplitude and (d) phase of $p_{\rm scatt}$ for $M=0.1$ and $\beta=0.5$. The cylindrical wave (40 acoustic periods at $f_0=500$ kHz) is emitted from $L_{\rm em}=-75$ mm. The amplitude is coded using a logarithmic gray scale: white is -10 dB and black is -180 dB in (a) and -120 dB in (c) relative to the maximum value of $p_{\rm scatt}$.

tered amplitude around the forward direction is much larger than that of the backscattered signal. Moreover, for $M=0.1$, the scattered wave is not symmetric about the y axis.

Finite-difference schemes also allow one to study the (quasi)monochromatic regime by using much longer emissions. Figure 17 presents the amplitude and the phase of the scattered pressure field $p_{\rm scatt}$ for a monochromatic cylindrical wave incident on a Taylor vortex. According to Ref. [44], we expect these results to be very close to those given by Lighthill's acoustic analogy [11]. For very small Mach numbers, the scattered amplitude displays a classical, quadrupolar pattern [Fig. 17(a)]. Outside a line of singularity in the forward direction, where $p_{\rm scatt}$ vanishes, the phase in Fig. 17(b) reveals that the scattered wave has a cylindrical structure as expected from theoretical and analytical approaches [11–17]. When M is increased for a given value of β, the scattered amplitude becomes asymmetric [Fig. 17(c)]. Moreover, Fig. 17(d) shows that the scattered wave for $M=0.1$ has a spiral structure. This feature was not pointed out in previous numerical studies, which focused on rms pressure levels or on directivity patterns [40,44]. Our simulation also reveals the presence of two defects in the phase pattern before the spiral wave fully develops in space. Such spiral solutions of the scattering problem have been predicted theoretically by Umeki and Lund [49] and observed experimentally in the interaction between surface waves and a vortex [50]. In the case of a finite-circulation vortex, such spiral waves are likely to be favored by the long-range advection effects that strongly distort the scattered wave at ''large'' Mach numbers. The present numerical results obtained for $\alpha=0.3$ and
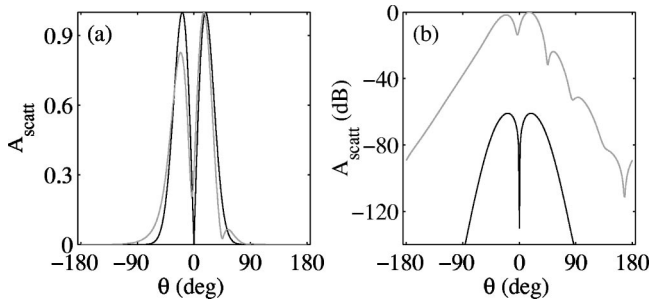
FIG. 18. Scattering amplitude vs the angle with the forward direction for $M = 10^{-4}$ (black) and $M = 0.1$ (gray) with $\beta = 0.5$. (a) Linear scale. (b) Logarithmic scale in dB. The directivity diagrams have been taken from Figs. 17(a) and 17(c) at $r = 30$ mm and rescaled by their own maximum in (a) and by the maximum amplitude obtained at $M = 0.1$ in (b).

3×10^{-4} with $\beta = 0.5$ constitute a useful complement to the analytical calculations by Coste, Lund, and Umeki [21], valid for $\alpha \approx 1$ and $\beta \gg 1/2\pi$.

Finally, the directivity patterns corresponding to Figs. 17(a) and 17(c) are plotted in Fig. 18. Not surprisingly, they are very similar to those obtained in Refs. [40,44] with a plane illumination. The peak scattering occurs at about $\theta = \pm 20°$ from the forward direction. No backscattering is observed at low Mach numbers and a strong asymmetry shows up for $M = 0.1$.

VII. CONCLUSIONS

The results presented in this paper are twofold. First, experimental data on the interaction between an ultrasonic wave and a strong vorticity filament have been successfully compared to analytical and/or numerical calculations, for both plane and cylindrical incident waves. Such calculations provide a nonintrusive method of measuring the intensity and size of a slender vorticity filament, which would be very difficult if not impossible with conventional techniques. Moreover, the use of transducer arrays allows fast and spatial measurements that turn out to be very interesting for studying transient regimes and the dynamics of vorticity.

Second, the case of a cylindrical incident wave has been studied in detail with a parabolic equation and a finite-difference numerical code. Such an investigation resulted from experimental motivations: cylindrical emission by a single element is cheaper, easier to control, does not require the use of two transducer arrays, and yields a more accurate measurement especially inside the vortex core. Our numerical results are similar to those of Refs. [21,40,44] but also uncover an original spiral solution for the scattered wave at ''large'' Mach numbers ($M = 0.1$ for $\beta = 0.5$). The crossover between cylindrical and spiral scattered waves as a function of M and β is currently under study.

As a global conclusion, we stress that the analysis of experimental data in the light of numerical simulations provides useful results for both the problem of remote sensing of vorticity filaments and the theoretical understanding of sound scattering by a vortex.

[1] D. W. Schmidt and P. M. Tilmann, J. Acoust. Soc. Am. **47**, 1310 (1970).

[2] R. H. Engler, D. W. Schmidt, W. J. Wagner, and B. Weitemeier, J. Acoust. Soc. Am. **71**, 42 (1982).

[3] W. Munk, J. Fluid Mech. **173**, 43 (1986).

[4] W. Munk, P. Worcester, and C. Wunsch, *Ocean Acoustic Tomography* (Cambridge University Press, Cambridge, 1995).

[5] R. H. Engler, D. W. Schmidt, and W. J. Wagner, J. Acoust. Soc. Am. **85**, 72 (1989).

[6] A. Hauck, Acoust. Imaging **18**, 317 (1991).

[7] R. Labbé and J.-F. Pinton, Phys. Rev. Lett. **81**, 1413 (1999).

[8] S. Manneville, A. Maurel, P. Roux, and M. Fink, Eur. Phys. J. B **9**, 545 (1999).

[9] S. Manneville, J.-H. Robres, A. Maurel, P. Petitjeans, and M. Fink, Phys. Fluids **11**, 3380 (1999).

[10] S. Douady, Y. Couder, and M.-E. Brachet, Phys. Rev. Lett. **67**, 983 (1991).

[11] M. J. Lighthill, Proc. R. Soc. London, Ser. A **211**, 564 (1952).

[12] A. L. Fetter, Phys. Rev. A **136**, 1488 (1964).

[13] S. O'Shea, J. Sound Vib. **43**, 106 (1975).

[14] A. L. Fabrikant, Akust. Zh. **28**, 694 (1982) [Sov. Phys. Acoust. **28**, 410 (1982)].

[15] P. V. Sakov, Akust. Zh. **39**, 537 (1993) [Acoust. Phys. **39**, 280 (1993)].

[16] J. Reinschke, W. Möhring, and F. Obermeier, J. Fluid Mech. **333**, 273 (1997).

[17] R. Ford and S. G. Llewellyn Smith, J. Fluid Mech. **386**, 305 (1999).

[18] Y. Aharonov and D. Bohm, Phys. Rev. **115**, 485 (1959).

[19] M. V. Berry, R. G. Chambers, M. D. Large, C. Upstill, and J. C. Walmsley, Eur. J. Phys. **1**, 154 (1980).

[20] F. Vivanco, F. Melo, C. Coste, and F. Lund, Phys. Rev. Lett. **83**, 1966 (1999).

[21] C. Coste, F. Lund, and M. Umeki, Phys. Rev. E **60**, 4908 (1999).

[22] P. Roux, J. de Rosny, M. Tanter, and M. Fink, Phys. Rev. Lett. **79**, 3170 (1997).

[23] J.-F. Pinton and G. Brillant (private communication).

[24] D. Blockintzev, J. Acoust. Soc. Am. **18**, 322 (1945).

[25] V. E. Ostashev, *Acoustics in Moving Inhomogeneous Media* (E & FN Spon, London 1997).

[26] R. H. Kraichnan, J. Acoust. Soc. Am. **25**, 1096 (1953).

[27] F. Lund and C. Rojas, Physica D **37**, 508 (1989).

[28] C. Baudet, S. Ciliberto, and J.-F. Pinton, Phys. Rev. Lett. **67**, 193 (1991).

[29] C. Baudet, O. Michel, and W. J. Williams, Physica D **128**, 1 (1999).

[30] R. Labbé, J.-F. Pinton, and S. Fauve, Phys. Fluids **8**, 914 (1996).

[31] S. Manneville, Ph.D. thesis, University Paris 7, 2000.

[32] S. Manneville, A. Maurel, F. Bottausci, and P. Petitjeans, *Structure and Dynamics of Vortices*, edited by A. Maurel and P. Petitjeans, Lecture Notes in Physics Vol. 555 (Springer-Verlag, Berlin, 2000), p. 231.

[33] M. Mory and N. Yurchenko, Eur. J. Mech. B/Fluids **6**, 729 (1993).

[34] R. Wunenburger, B. Andreotti, and P. Petitjeans, Exp. Fluids **27**, 181 (1999).

[35] L. D. Landau and E. M. Lifshitz, *Fluid Mechanics* (MIR, Moscow, 1989).

[36] B. Andreotti, Ph.D. thesis, University Paris 7, 1999.

[37] N. Mordant, J.-F. Pinton, and F. Chillà, J. Phys. II **7**, 1729 (1997).

[38] P. G. Saffman, *Vortex Dynamics* (Cambridge University Press, Cambridge, 1992).

[39] S. Olariu and I. Iovitzu Popescu, Rev. Mod. Phys. **57**, 339

[40] S. M. Candel, J. Fluid Mech. **83**, 465 (1979).

[41] V. E. Ostashev, D. Juvé, and P. Blanc-Benon, Acust. Acta Acust. **83**, 455 (1997).

[42] P. Roux, H. C. Song, M. B. Porter, and W. A. Kuperman, Wave Motion **31**, 181 (2000).

[43] M. D. Collins, J. Acoust. Soc. Am. **96**, 382 (1994); **93**, 1736 (1993).

[44] T. Colonius, S. K. Lele, and P. Moin, J. Fluid Mech. **260**, 271 (1994).

[45] C. Bailly and D. Juvé, AIAA J. **38**, 22 (2000).

[46] R. Berthet (private communication).

[47] B. T. Chu and L. S. G. Kovásznay, J. Fluid Mech. **3**, 494 (1958).

[48] F. Collino, Institut National de Recherche en Informatique et en Automatique Report No. 1790, 1993 (unpublished).

[49] M. Umeki and F. Lund, Fluid Dyn. Res. **21**, 201 (1997).

[50] F. Vivanco and F. Melo, Phys. Rev. Lett. **85**, 2116 (2000).

(1985).